A multilevel theoretical study to disclose the binding mechanisms of gold(III) bipyridyl compounds as selective aquaglyceroporin inhibitors

Valentina Graziani,[a] Alessandro Marrone,[a,*] Nazzareno Re,[a] Cecilia Coletti[a]
James A. Platts,[b] Angela Casini[b]

Addresses:

[a]Università "G d'Annunzio" di Chieti-Pescara, Department of Pharmacy, Via dei Vestini 31, 66100, Chieti, Italy

[b]School of Chemistry, Cardiff University, Park Place, Cardiff CF10 3AT, U.K.

Corresponding authors:

Dr. Alessandro Marrone: amarrone@unich.it

Abstract

Structural studies have paved the avenue to a deep understanding of AQPs, small ancient proteins providing efficient transmembrane pathways for water, small uncharged solutes as glycerol, and possibly gas molecules. Despite the numerous studies, their roles in health and disease remain to be fully disclosed. The recent discovery of Au(III) complexes as potent and selective inhibitors of *aquaglyceroporins* isoforms paves the way to their possible therapeutic application. The binding of the selective human AQP3 inhibitor, the cationic complex $[Au(bipy)Cl_2]^+$ (Aubipy), with the protein channel was investigated here by means of a multilevel theoretical workflow including QM, MD, and QM/MM approaches. The hydroxo complex was identified as the prevalent form of Aubipy in physiological media and its binding to AQP3 studied by MD. Both non-covalent and coordinative Aubipy-AQP3 adducts were simulated to probe their role in the modulation of water channel functionality. The electronic structure of representative Aubipy-AQP3 adducts was then analysed to unveil the role played by the metal moiety in their stabilization. This study spotlights the overall importance of three key aspects for AQP3 inhibition: 1) water speciation of Au(III) complex; 2)

stability of non-covalent adducts; 3) conformational changes induced within the pore by the coordinative binding of Au(III). The obtained results are expected to orient future developments in the design of isoform selective Au(III) inhibitors.

Introduction

Aquaporins (AQPs) are a family of small hydrophobic integral transmembrane water channel proteins involved in transcellular and transepithelial water movement.[1] AQPs are ubiquitous in all domains of life and can be functionally categorized into two major subgroups, mainly determined by their transport capabilities: i) orthodox aquaporins, which are water-specific channels, and ii) aquaglyceroporins, allowing permeation of water but also of non-polar solutes, such as glycerol and other polyols, urea, the reactive oxygen species hydrogen peroxide, as well as ammonia, metalloids and gases (e.g. carbon dioxide). In mammals, the 13 aquaporin isoforms identified so far (AQP0-12) are expressed in a wide range of tissues and are involved in many biological functions.

AQPs share a common protein fold, with the typical six membrane-spanning helices surrounding the 20-Å-long and 3-4-Å-wide amphipathic channel, plus two half-helices with their positive, N-terminal ends located at the centre of the protein and their C-terminal ends pointing towards the intracellular side of the membrane.[2] The selectivity of AQPs' transport of specific solutes is guaranteed, in all organisms, by the presence of two constriction sites. Firstly, an aromatic/arginine selectivity filter (ar/R SF) near the periplasmic/extracellular entrance that, in water-specific aquaporins, is approximately 2.8 Å in diameter (identical to that of a water molecule) and about 3.4 Å in aquaglyceroporins (matching the diameter of a carbon hydroxyl group of polyols such as glycerol). Secondly, a constriction site composed of two conserved asparagine-proline-alanine (NPA) sequence motifs, located at the N-terminal ends of the two half-helices, at the centre of the channel. Overall, the conduction pores of AQPs are roughly 25 Å long and both constriction sites interact strongly with water. In humans, functional aquaporins are organized in a tetrameric structure.

Due to their numerous roles in physiology, these proteins are essential membrane transporters involved in crucial metabolic processes and expressed in almost all tissues. Analyses of transgenic mice have revealed potential roles of aquaglyceroporins in skin elasticity, gastrointestinal function and metabolism, and metabolic diseases such as diabetes mellitus. Furthermore, they appear to be involved in cell proliferation, carcinogenesis, and fat metabolism. The functional significance of

glycerol transport by aquaglyceroporins has been the subject of several studies. For example, numerous evidences suggest that the expression of AQP3 is tightly correlated with cell proliferation and migration. Hara-Chikuma and Verkman showed the knockout of AQP3 could affect the proliferation and migration ability of keratinocyte and slow the wound healing rate of mouse skin. [3] However, when the expression of AQP3 was upregulated in human keratinocytes by transfection with human AQP3 DNA plasmid, cell proliferation was increased. [4] Various other studies have shown the relationship between AQP3 expression and cancer development. [1,5,6]

With the aim to validate the hypotheses on the various roles of AQPs in health and disease, in addition to genetic approaches, the use of inhibitors to unravel aquaporin function holds great promise. However, no reported AQP inhibitors possess so far adequate features for clinical development due to insufficient isoform selectivity.[7] Within this context, the effect of sulfhydryl-reactive compounds such as $HgCl_2$ on water and glycerol permeability inhibition via AQPs is well described in the literature; however, these metal compounds are typically used to identify AQP activity in biochemical assays, but are also extremely toxic and non-specific, and therefore, not suitable for therapeutic application.

In 2012, we reported for the first time on the potent and selective inhibition of human AQP3 by a series of gold(III) coordination compounds with nitrogen-donor ligands. [8] Interestingly, the compounds could potently inhibit glycerol transport through hAQP3 in human red blood cells (hRBC), while they were not active on water transport via the orthodox water channel human AQP1. The most potent inhibitor of the series, Auphen ($[Au(phen)Cl_2]Cl$, phen = 1,10-phenanthroline), was shown to have an IC_{50} in the low micromolar range (0.8 ± 0.08 μM) and was far more effective than the mercurial compound $HgCl_2$ in inhibiting AQP3.[8]

Inspired by these initial promising results, we investigated other gold-based compounds as possible AQP3 inhibitors, [9] to achieve initial structure-activity relationships. For example, a family of square planar gold(III) complexes containing functionalised bipyridine ligands of the general formula, $[Au(N\hat{}N)Cl_2][PF_6]$ (Aubipy, where N^N = substituted 2,2'-bipyridine) was tested. Notably, all the gold(III) complexes were effective inhibitors of glycerol permeability via AQP3, with an IC_{50} in the low μM range, and comparable in potency to Auphen.[10]

To further study the mechanisms of aquaglyceroporin inhibition by gold compounds a homology model of human AQP3 was built, allowing the identification and characterization of protein binding pockets and possible binding sites. [8] According to the hard and soft

(Lewis) acids and bases (HSAB) theory, gold has high affinity for binding to sulphur-containing nucleophiles. Thus, the mechanism of AQP3 inhibition by Auphen and analogues is likely to be based on the ability of Au(III) ions to interact with the thiol of cysteine or the thioether of methionine residues in proteins. In AQP3, only the thiol group of cysteine-40 (C40) located just above ar/R SF inside the protein channel is accessible for gold binding, being projected towards the extracellular space. Molecular docking studies showed that positioning of the compound in close proximity of C40 was possible; [8] thus, rendering the direct binding of Au(III) to this residue, upon release of one of the chlorido ligands, very probable. Additional QM/MM calculations, provided evidence that the ligand moiety may play a major role in selectivity towards this isoform, as ligand substituents can interact with other amino acid side-chains lining the aquaporin channel, stabilizing the position of the inhibitor in the binding pocket.[10] Notably, site-directed mutagenesis studies in transfected cells provided evidence that mutation of C40 to S40 in human AQP3 significantly decreased the inhibitory effects of Auphen on glycerol permeability via AQP3.[11]

Furthermore, the mechanism of AQP3 inhibition of water and glycerol permeation by another gold(III) complex - $[Au(PbImMe)Cl_2]PF_6$ (PbImMe = 1-methyl-2-(pyridin-2-yl)-benzimidazole) has been recently described using molecular dynamics (MD), allowing elucidation of important structural changes leading to pore closure upon gold binding.[12] Specifically, these results allowed discovering that protein conformational changes, upon metal binding to C40 in human AQP3, are mostly responsible for the observed inhibition of water and glycerol permeation, instead of direct steric hindrance of the substrate molecules by the gold complex.

Despite these initial studies, the mechanisms of AQP inhibition by gold(III) complexes needs further attention. The interaction of metal drugs with the physiological environment is often accompanied by modification of the metal coordination sphere via ligand exchange processes. As an example, anticancer Pt(II) drugs like cisplatin or carboplatin are activated by aquation through the formation of more reactive aquo species.[47] On the other hand, Au(III) complexes, although sharing structural features with Pt(II) anticancer compounds, act as protein binders and are mostly found bound to sulphur nucleophilic sites such as the thiol side chain of cysteine residues.[13] A possible explanation for the protein-selectivity of Au(III) complexes may be the different speciation in water of these compounds that modulates the reactivity of the metal centre by inducing a higher affinity for the thiol groups of cysteine

with respect to other amino acids. Moreover, previous QM/MM studies established the importance of the aromatic ligands of Au(III) for reactivity with AQP3 via the establishment of non-covalent interactions within the extracellular side of the pore. [10] To probe these issues in more detail, we combined DFT calculations to MD simulations and QM/MM studies to examine the chemical processes leading to binding at the extracellular pore of AQP3 of the selected inhibitor $[Au(N^N)Cl_2][PF_6]$ (Aubipy, where N^N is 2,2'-bipyridine). This Au(III) complex was selected within the "bipy" family to explore the binding features of the most basic scaffold within the AQP3 pore, which should further orient future inhibitor design. Notably, MD approaches have already proved of extreme importance to investigate the physiological mechanisms of substrate transport by AQPs, as well as of AQPs inhibition by small molecules.[14]

Three aspects of Aubipy-AQP3 binding process were specifically explored in the present study: i) the speciation mechanisms of Aubipy in physiological environment, including aquation, deprotonation, and thiol binding, using DFT; ii) characterization of the non-covalent (reversible) or coordinative (irreversible) adducts between AQP3 Aubipy through MD simulations; iii) the electronic structure of Aubipy-AQP3 adducts via combination of QM/MM optimization, Atoms-In-Molecule (AIM), and Natural Bond Orbitals (NBO) approaches. This approach allowed us to gain a detailed insight into the molecular events leading to the binding and inhibition AQP3 by Aubipy, and spotlights the role played by the Au(III) centre in the isoform selectivity disclosed by this family of aquaglyceroporins inhibitors. We expect the presented computational results to be a viable support in the development of new gold(III)-based aquaporin modulators.

Experimental Section

DFT studies. All calculations were performed by using the Gaussian 09 package.[15] The local minimum geometry of each Au(III) and Pt(II) species (see below) was calculated with the hybrid exchange-correlation functional B3LYP,[16] shown to be suitable for these systems,[17] and the following basis sets scheme: the basis set labelled by the LANL2DZ keyword describes the valence shell electrons of Au, Pt, S, and Cl with a double-ζ plus one l+1 polarization basis set and uses a pseudopotential to take into account the relativistic effects affecting the core electrons,[18] and the all-electron 6-31G* by Pople[19] employed to treat the remaining atoms; we hereafter denote this

basis set scheme with sbs (small basis set). The conductor-like screening model implemented in Gaussian 09 (CPCM [20]) was used in the calculation of local minima to simulate the effect of a water bulk (with default settings for water). Vibrational frequencies analyses were performed at the same level of theory (CPCM/B3LYP/sbs) to confirm the correct nature of the optimized stationary points and calculate zero-point energy and thermal corrections (under the hypothesis of an ideal gas behaviour) for enthalpy and free energy estimates.

The electronic energy of each CPCM/B3LYP/sbs geometry was recalculated by using a larger basis set scheme: i) the all-electron triple-ζ 6-311G+(d,p) basis set including one l+1 polarization plus one s diffusion function for C, N, O, and H;[21] ii) the analogous 6-311G+(3d) basis set for Cl;[21] iii) Au and Pt core electrons were described again through the LANL2 pseudo-potential[18] while for valence shell we used a fully uncontracted (5s, 5p, 3d) Gaussian basis set[22] plus an f polarization function with an exponent coefficient of 1.050 and 0.993 for Au and Pt, respectively. We hereafter denote this basis set scheme with lbs (large basis set).

Reaction thermodynamics. For each species X, the free energy in water solution at 298 K ($G_x^0(sol)$) was computed as:

$$G_x^0(sol) = E_x^{lbs}(sol) + G_{x,corr}^{sbs}$$

Where, $E_x^{lbs}(sol)$ is the electronic energy calculated at CPCM/B3LYP/lbs//CPCM/B3LYP/sbs level of theory and $G_{x,corr}^{sbs}$ is a correction term comprising the zero-point energy, and the enthalpy and entropy corrections. The only exception was represented by the chloride ion:

$$G_{Cl-}^0(sol) = E_{Cl-}^{lbs}(gas) + \Delta G_{Cl-,solv}^{\exp} + G_{x,corr}^{sbs}$$

for which an experimentally determined value of solvation free energy ($\Delta G_{Cl-,solv}^{\exp}$)[23] was used in place of the corresponding CPCM value. The free energy values for each molecular species were then combined according to the thermodynamic cycles depicted in Schemes S1-S3 to calculate the reaction free energies for the investigated processes.

pKa estimations. A semi-empirical approach was employed for the estimate of the pKa values of both aquo and thiol-coordinated complexes based on the calculation of proton exchange free energies. $G^0\,(sol)$values at CPCM/B3LYP/lbs//CPCM/B3LYP/sbs level of theory were calculated for a

set of ten aquo complexes (Supporting Information, Note 1), in either undissociated and dissociated form, and with assigned experimental values (pKa^{exp}). We then considered the thermodynamic decomposition depicted in Scheme 3 by which the following relation can be derived:

$$\Delta G^{theo}_{HA,deprot} = \Delta G^{theo}_{HA/ref^-,exch} + \Delta G^{exp}_{Href,deprot}$$

where HA denotes any aquo complex in the set, $Href$ is a reference aquo complex used to measure the deprotonation of any other complex in the set, $\Delta G^{theo}_{HA/ref^-,exch}$is the free energy for the proton exchange between HA and ref^-, and $\Delta G^{exp}_{Href,deprot}$ is the experimentally derived deprotonation free energy. In this study, $Href$ and ref^- species correspond to chloro-aquo-diammino platinum and chloro-hydroxo-diammino platinum, respectively. The values of pKa^{exp} were then regressed against the pKa^{theo} values of any HA in the set. The regression model eventually employed for the estimation of pKa of Au(III) species was:

$$pKa^{est}_{HA} = a \cdot pKa^{theo}_{HA} + b \qquad R^2 = 0.9266$$

where b = 2.8421 and a = 0.5367. (See Supporting Information for further details).

Reaction kinetics. For all ligand exchange processes involving Pt(II) or Au(III) species, an associative-interchange mechanism was taken into account. The molecular systems corresponding to reactant (RA) or product (PA) adducts were calculated as local minima of the CPCM/B3LYP/sbs potential energy surface (PES), interconnected by first-order saddle points corresponding to transition state (ts) structures. The correct nature of each PES stationary point was checked by ascertaining that the hessian matrix of minimum or saddle points were featured by 0 or 1 negative eigenvalues, respectively. Intrinsic reaction coordinate (IRC) calculations were performed to check the correct interconnection of each ts point to the expected RA and PA species. The CPCM/B3LYP/sbs structures intercepted along the reaction channel were further subject to single point calculations at CPCM/B3LYP/lbs for the estimate of the free energies at 298 K and in water solution as described in the previous section. The activation free energy of any ligand exchange reaction was obtained with the assumption of RA→ts as the rate determining step. Relaxed scan calculations along internal coordinates resembling the expected RA→ts coordinate were also performed in the search of ts structure for the Cl^- →CH_3S^- substitution in $[Aubipy(OH)Cl]^+$ for which localization resulted to be particularly challenging (Figure S1).

MD simulations. The binding of Au(III) complexes at the extracellular pore of AQP3 was investigated by means of classical molecular dynamics (MD). All molecular systems consisted of an AQP3 tetramer soaked into a double layer of palmitoyl-oleyl-phosphatidyl-coline (POPC), and globally sandwiched by two layers of water molecules. The initial structure of each AQP3 monomer had already been obtained by comparative homology modelling and previously reported.[8] Three different binding states of one AQP3 unit were then taken into account for the simulation of three corresponding Au(III)-AQP3 systems: A) unbound; the C40 side chain was assumed in its SH neutral form; B) non-covalently bound, obtained by placing the Au(III) species into the extracellular pore by means of docking approaches[7-9] followed by simulation of the resulting system with no other constraints; again, C40 was considered in its neutral form. The last trajectory snapshot from this simulation was used to generate the input for the simulation of the covalent adduct C) covalently bound. Firstly, a steered MD scheme was applied to the last snapshot of non-covalent complex trajectory to gradually approach the Au(III) metal fragment to the side chain of C40. We used a direction-constrained pull-code procedure for the application of a force of constant 1000 kJ mol^{-1} nm^{-2} and rate of 0.5 nm ns^{-1} to the distance between the Au(III) centre (point of application) to the sulfur atom of C40. The steered MD simulation was performed for 3 ns (150000 steps of 2 fs) by progressively shortening the Au-S distance in the non-covalent adduct (14.4 Å) until reasonably close to the expected value for a covalent bond (in the range of 2.5-3.0 Å). The last snapshot of steered MD trajectory was then modified by removing of the C40 thiol proton (the expected coordinated form as indicated by DFT calculations: see Results) and including the covalent Au-S bond in the system topology, to eventually obtain the starting model of covalent AubipyOH-AQP3 complex.

All molecular systems were simulated in the all-atom Amber force field [24] by using Gromacs.[25] Parameters for the Au(III) species were either *de novo* calculated or assigned by adapting existing parameters. Bonded and non-bonded parameters describing the structure of the bipyridyl ligands were retrieved from the Amber parameter set available in the Gromacs software, while those describing the square-planar metal complexes were obtained by DFT approaches as indicated in ref 11 (Supporting information, Note 3). The employed MD scheme was largely retrieved and adapted to the Aubipy-AQP3 specific features from the work of Spinello et al. [26] and by the use of the charmm-gui web-server. [27,28] Briefly, the double layer was made of 166 POPC molecules (88+88) completed with about 17000 water molecules. Each AQP3 tetramer, made up of four protein chains (monomer I-IV), was then placed at the centre of the POPC double layer + water by using the charmm-gui tools[27,28] and simulated in a cubic box with approximate volume of 99^3 $Å^3$ within the following scheme: i) local energy minimization; ii) slow heating: six MD runs with a time step of 1 fs

(25 ps) in which the protein temperature was set at 0, 100, 150, 200, 250, and 300 K; ii) production runs with a time step of 2 fs (200 ns) at 300 K in an isothermal/isobaric ensemble, using Nose-Hoover (temperature) and the semiisotropic Parinello-Raman coupling scheme (pressure).[29,30] The LINCS algorithm was adopted to constrain all bond lengths,[31] and the long range electrostatics were computed by the Particle Mesh Ewald method.[32] Trajectory analyses were carried out by using suitable Gromacs utilities with the support of either VMD or Maestro graphical interfaces.[33,34] The HOLE program[35] was used in the calculation of AQP3 monomer **I** channel radius, by setting an end radius of 5.0 Å and constraining the estimation to the z axis vector. Channel radii of monomer **I** from A, B, and C systems were calculated on 1000 snapshots sampled from the last 100 ns of each trajectory. An in-house Perl script was then used to calculate the average channel radii reported in Figure 3. Trajectory analyses were also performed to estimate the effects of Aubipy binding on water permeation. The time-averaged water density along the channel direction was calculated by using the density tool of Gromacs. The flux (p_f) of water was calculated by using the collective diffusion model reported by Zhu et al. [36]:

$$p_f = \frac{V_w}{N_A} D_n$$

with V_w, N_A, and D_n corresponding to the water molar volume ($cm^3\ mol^{-1}$), the Avogadro number (mol^{-1}), and the water diffusion coefficient (s^{-1}), respectively. The diffusion coefficient can be calculated from an equilibrated trajectory through the mean-square displacement of intra-channel confined water molecules expressed by using the collective variable *n(t)*:

$$< n^2(t) >= 2D_n t + C$$

where C is a constant. [37] The calculation of $<n^2(t)>$ for the water confined in the monomer I channel (see below) was performed by using the msd tool of Gromacs over the last 2 ns of trajectory; D_n was directly provided by this tool by fitting the above equation over 201 time restarts.

The monitoring of the hydrogen bonds formed by R218 in the equilibrated (last 100 ns) segment of A-C trajectories was performed by using the *hydrogen bond* tool implemented in the VMD graphical user interface.[33] For all three systems, hydrogen bond detection was performed on the partition including whole residues within a radius of 6.0 Å from the guanidine carbon of R218 of monomer I, and by setting the criteria for hydrogen bond assignment at 3.0 Å and 20° for threshold heavy atoms distance and critical angle deviation, respectively. The frequency of each unique hydrogen bond was eventually expressed by the ratio (reported in percentage) of the number of detections over the total number of scanned snapshots (1000: one per 100 ps in the last 100 ns of trajectory).

The most representative AQP3-bound conformations were extracted from B and C system trajectories by clustering analysis. The Daura method [38] was applied to cluster the last 100 ns of each trajectory with respect to the position of either metal moiety, i.e. $[Aubipy(OH)Cl]^{+}$ and $[Aubipy(OH)]^{2+}$ for B and C system, respectively, and a system partition composed of 40-63, 134-148, and 212-218 sequence segments. These segments were selected to i) include protein residues within 3.0 Å from the metal fragment in either B or C system, and ii) partition the protein systems into a minimum number of peptide fragments, thus resulting in partitioned systems with limited truncations. For consistency, system A was also clustered on the same protein partition. The middle elements of each cluster are then selected to form a set of conformations representative of either bound or unbound status of AQP3. For each system, a subset was obtained with the middle elements of most populated clusters covering at least 90% of the whole ensemble; each subset element was also assigned with a normalized weighting factor. Finally, each subset element underwent local energy minimization in the Gromos force field by the application of harmonic forces of 1000 and 100000 kJ mol^{-1} nm^{-2} to constrain the positions of the backbone Cα and metal fragment atoms, respectively.

QM/MM calculations. QM/MM calculations were performed with the two-level ONIOM method within the Gaussian09 suite of programs.[39] The DFT method with the B3LYP hybrid functional[16] was used for the high layer, coupled with the FF96 force field of Cornell et al. (AMBER) for the low layer.[40] A basis set consisting of 6-31+G(d,p) on light atoms and Stuttgart–Dresden (SDD) basis set and effective core potential on Au was employed.[41] Partitioning of the layers was achieved by hydrogen link atoms replacing carbon at the Cα-Cβ bond of the cysteine residue to which Aubipy binds. QM/MM calculations were addressed on the most representative structures obtained from non-covalent and covalent Aubipy(OH)-AQP3 adducts, *i.e.* B1 and C1, respectively. To reduce the computational burden, B1 and C1 structures were partitioned by including only the amino acid residues (total 61) and water molecules (up to 11) within a radius of about 16 Å from the metal fragment positions. Initial geometry optimization of these MD structures was carried out by using a small QM region consisting of the $[Aubipy(OH)Cl]^{+}$ complex for the B1 model and the Aubipy(OH)–Sγ–CβH_2fragment, with link H-atom replacing Cα of C40, for the C1 model. All atoms in the QM layer were unconstrained whereas only the Cα atomic coordinates in the MM layer were frozen.

Coordinates of metal complex, neighbouring amino acids and water molecules were extracted from QM/MM optimised geometry and treated with DFT, also in Gaussian09. Natural bond orbital (NBO) [42] and Quantum Theory of Atoms in Molecules (QTAIM) [43] analysis was performed at B3LYP/6-

31+G(d,p)-SDD level. Binding energy between Aubipy (or fragments thereof) was performed using wB97x-D[44]/6-31+G(d,p)-SDD and corrected for BSSE using counterpoise method.[45]

Results and Discussion

Reactions of Aubipy in physiological environment: a DFT study. Aubipy is a monocationic, square-planar complex formed by the coordination of a bipyridyl ligand and two chlorides to an Au(III) ion. Consistently with experimental data reported elsewhere, [46] we considered ligand exchange processes of the two labile chlorido ligands, involving the reaction with water or other suitable nucleophiles. Specifically, the reaction of Aubipy species with methanethiol was investigated because this molecular fragment resembles the side chain of cysteine residues, known to be likely binding sites for Au(III) complexes. [8] Estimation of the thermodynamic parameters was performed by the use of DFT approaches and by adopting the same reaction decomposition scheme for the investigated substitution reactions with water or methanethiol, respectively (Scheme 1).

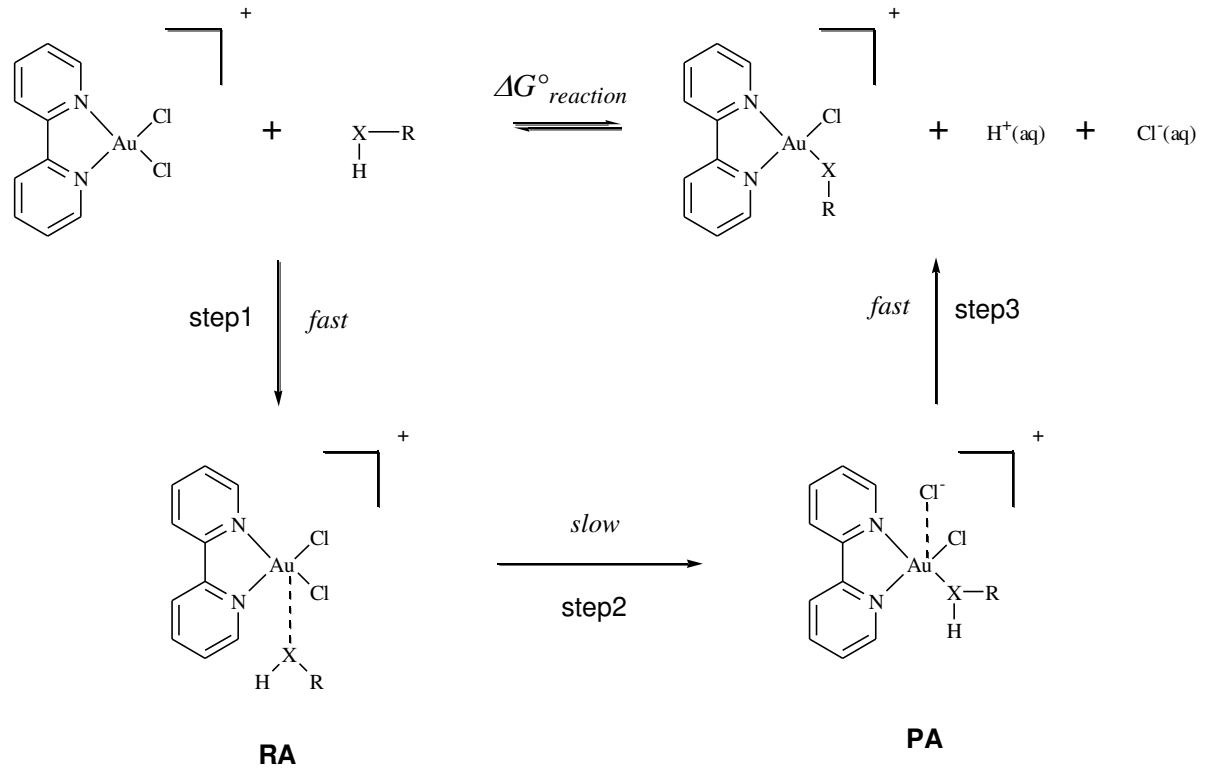

Scheme 1. Reaction decomposition scheme for the substitution of the chlorido ligands in Aubipy. X = O, S and R = H, CH_3.

The adopted decomposition scheme suited for protic nucleophiles allowed convenient separation of the reaction free energy into three contributions. Step 1 and step3 are characterized by a high contribution of solvation entropy, so that the corresponding free energy terms were better estimated through the addition of empirical parameters. Indeed, step 1 was in turn decomposed into three sub-steps and the corresponding free energy contribution could be thus expressed:

$$\Delta G^{0}_{step1} = -\Delta G^{0\,Aubipy}_{solv} + \Delta G^{0\,H_2O}_{vap} + {}^{\mathrm{gas}}\Delta G^{0}_{step1} + \Delta G^{0\,Aubipy*H_2O}_{solv}$$

including the experimental term $\Delta G^{0\,H_2O}_{vap}$ (Scheme S1). Empirical terms were also included in the estimation of the free energy values for the formation of H^+ and Cl^- in water that contribute to the free energy for step 3 (Scheme S2-S3). These two steps are also expected to be fast by consisting in the mutual approach/detachment of molecular fragments and, thus, irrelevant in determining the reaction rate. On the other hand, step 2 corresponds to a pseudo-molecular rearrangement involving the cleavage/formation of covalent bonds in reactant and product adducts, RA and PA, respectively, more likely determining the rate of the whole process.

This general scheme was herein adapted to the investigation of either aquation, R=H and X=O, or thiol binding, R=CH_3 and X=S. In both cases, we assumed step 3 affording the deprotonation of the substitution product, because calculations indicate a strong increase in acidity for the X–H bond upon coordination on the Au(III) metal centre. Indeed, negative *pK*a values (Supporting Information, Note 1) were estimated for the putative aquo or thiol complexes, so that these species can be considered negligible at equilibrium. The free energy profiles for substitution of chlorido ligands in Aubipy with water (aquation) are reported (Scheme 2).

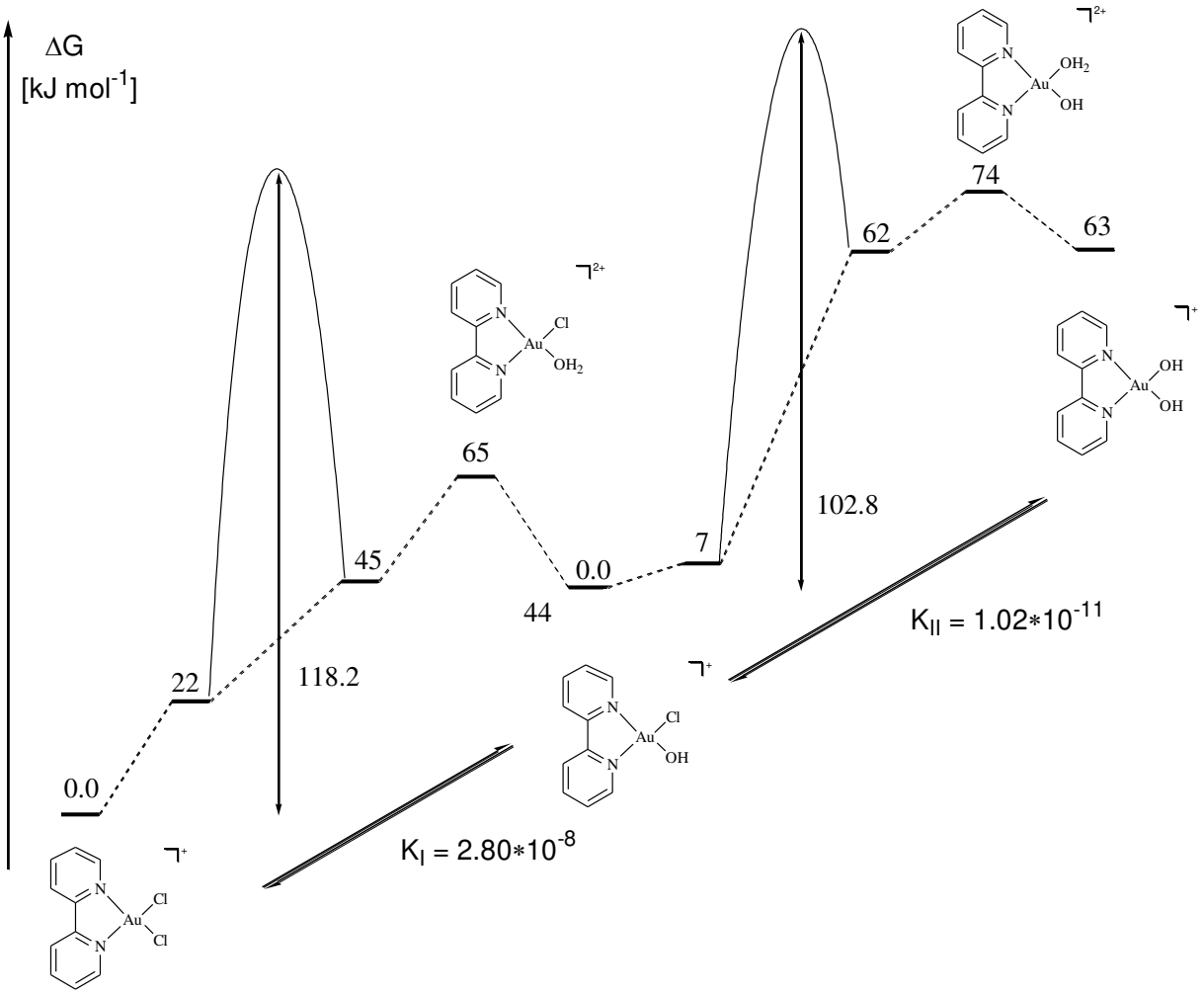

Scheme 2. Free energy profiles for the first and second aquation of Aubipy.For sake of clarity free energy values for the second aquation were rescaled by the energy of the first aquation products, i.e. by 44 kJ mol^{-1}.

Both first and second aquation steps of Aubipy are endoergonic processes, thus corresponding to left-shifted equilibria. While the combination of step 3 with deprotonation of the aquo species led to almost null contribution, most of the endoergodicity is ascribed to step 1 and step 2. The estimated thermodynamic constants for the first and second aquation of Aubipy allowed estimation of the speciation of this complex in water at physiological conditions characterized by constant pH of 7.4, hence with a hydrogen ion concentration of 3.98×10^{-8} M, and constant chloride concentration of 100 mM. Consistently with our theoretical estimations, we obtained:

$$\frac{[AubipyCl(OH)]}{[Aubipy]} = 11.457 \qquad \frac{[Aubipy(OH)_2]}{[AubipyCl(OH)]} = 5.126 \times 10^{-3}$$

The concentration trend Aubipy(OH)Cl (91.5%) >AubipyCl_2 (8.0%) >Aubipy$(OH)_2$ (0.5%) highlights the mixed chloro-hydroxo species as the dominant species for the reaction with endogenous targets. Accordingly, the reaction of Aubipy(OH)Cl with methanethiol, as a model of the cysteine side chain, was investigated by adopting the same computational approach.

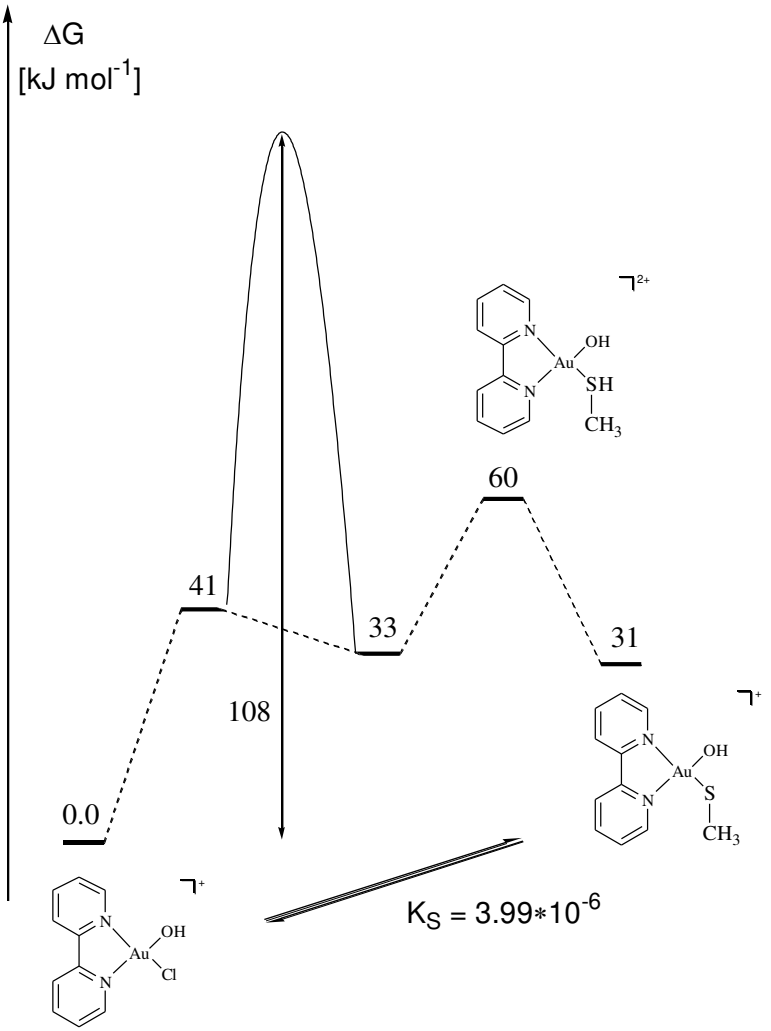

Scheme 3. Free energy profiles for the reaction of Aubipy(OH)Cl with methanethiol.

Although to a lesser extent compared to aquation, chloride substitution by methanethiol is endoergodic and leads to a left-shifted equilibrium (Scheme 3). However, in this case, endoergodicity is entirely caused by step 1 corresponding to the non-covalent approach of the nucleophile on the Au(III) coordination sphere, while step 2 and 3 are slightly exoergodic.

On the other hand, calculation of activation free energy values for step 2 of either aquation or thiol binding reaction shows that these processes are affected by a kinetic barrier around 100 kJ mol^{-1},

very similar to those reported for the anticancer drug cisplatin [47], and, analogously, are subjected to a kinetic control. In this comparison, we computed the activation free energy of the complete reaction by the sum of the reaction free energy for step 1 and the activation free energy of step 2 (Supporting Information, Note 2 and Table S2). Analysis of ligand exchange processes involving Aubipy species clearly spotlighted the overall importance of chloride substitution, ruling out the formation of more reactive aquo species. The kinetic control of both aquation and thiol binding is another important feature of Aubipy reactivity, because it possibly increases the significance of non-covalent adducts with potential endogenous targets.

In summary, consistent with the proposed decomposition scheme, the reaction of Aubipy bearing at least one chlorido ligand, i.e. AubipyCl, with a general H–X–R nucleophile can be depicted in three steps as depicted in Scheme 4.

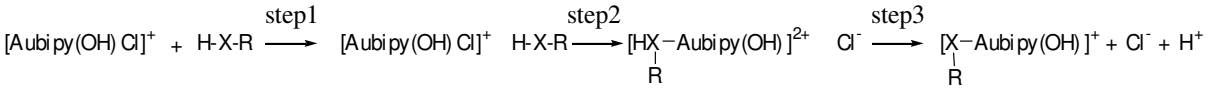

Scheme 4. Decomposition of the binding of a protic nucleophile at the metal centre of [Aubipy(OH)Cl]$^+$.

At variance from *cis*-Pt(II) complexes, Aubipy aquation leads to the corresponding chloro-hydroxo species which are likely to react with endogenous targets. The substitution of chlorido by hydroxo ligands may have a significantly different impact on the reactivity of metal complexes towards nucleophiles when different metal centers are concerned. Indeed, as shown by our calculations, the basicity of hydroxo groups at Au(III) centre is negligible (pKa < 0),whereas the hydroxo species of Pt(II) complexes such as cisplatin are sensibly more basic – for example the pKa of $[Pt(NH_3)_2(H_2O)_2]^{2+}$ and $[Pt(NH_3)_2Cl(H_2O)]^+$is 5.5 and 6.6, respectively – and may, consequently, be protonated back to their aquo forms reputed to be the actual DNA-targeting species.[47] Accordingly, aquation does not activate, but rather narrows, the reactivity of the Au(III) centre by the substitution of one scissile $Cl^–$ with a more inert $OH^–$ ligand, so that bipyridyl-Au(III) complexes can likely form only mono-functional rather than bifunctional adducts with their targets. Therefore, the moderately high kinetic barriers for either second aquation or thiol binding of [Aubipy(OH)Cl]$^+$ suggest that the formation of non-covalent adducts may be important in the early stages of the AQP3 binding. The formation of such adducts that favor the approach of the Au(III) centre in proximity of the thiol binding site is

expected to facilitate, both thermodynamically and kinetically, the formation of the covalent adduct. Indeed, DFT calculations showed that most of the endoergodicity related to the thiol binding of Aubipy(OH)Cl^+ is ascribed to step 1, corresponding to the formation of a non-covalent adduct.

Thus, the non-covalent interaction of [Aubipy(OH)Cl]$^+$ with residues of the extracellular pore of AQP3 may compensate the endoergodicity related to the approach of the metal centre and thiol, thus making the formation of coordinative adducts both thermodynamically and kinetically more favoured. DFT calculations also allowed to predict that endogenous targets may form non-covalent adducts with [Aubipy(OH)Cl]$^+$ if the target-ligand interaction energy is higher than 40 kJ mol^{-1}, which is approximately the amount of endoergodicity related to step 1 of thiol binding.

Aubipy(OH)-AQP3 adducts formation elucidated by MD simulations. In order to gain further insights into the physiological mechanisms of AQP3 inhibition by Aubipy, we applied MD simulations. The 3D structure of one AQP3 monomer had been already obtained by comparative homology modelling approaches and reported elsewhere. [7-9] This structure was used to build up the molecular system dealt with in the present investigation, consisting of an AQP3 tetramer soaked into a POPC double layer and further sandwiched into two water layers. MD investigations were carried out on three molecular systems differing for the binding state of AQP3. System A comprehended all unbound AQP3 monomers. System B was assembled by inserting one [Aubipy(OH)Cl]$^+$ complex in proximity of the extracellular pore of one AQP3 monomer. System C was obtained by the use of a steered MD approach to connect a [Aubipy(OH)]$^{2+}$ to the C40 side chain (in the thiolate form) forming a Au–S bond: system A, B, and C correspond to unbound, non-covalent, and covalent Aubipy-AQP3 complex, respectively. All systems share the same topology and spatial orientation with the z axis perpendicular to the double POPC layer, i.e. approximately parallel to the channel, and directed from extracellular to cytoplasmic pore (Figure 1).

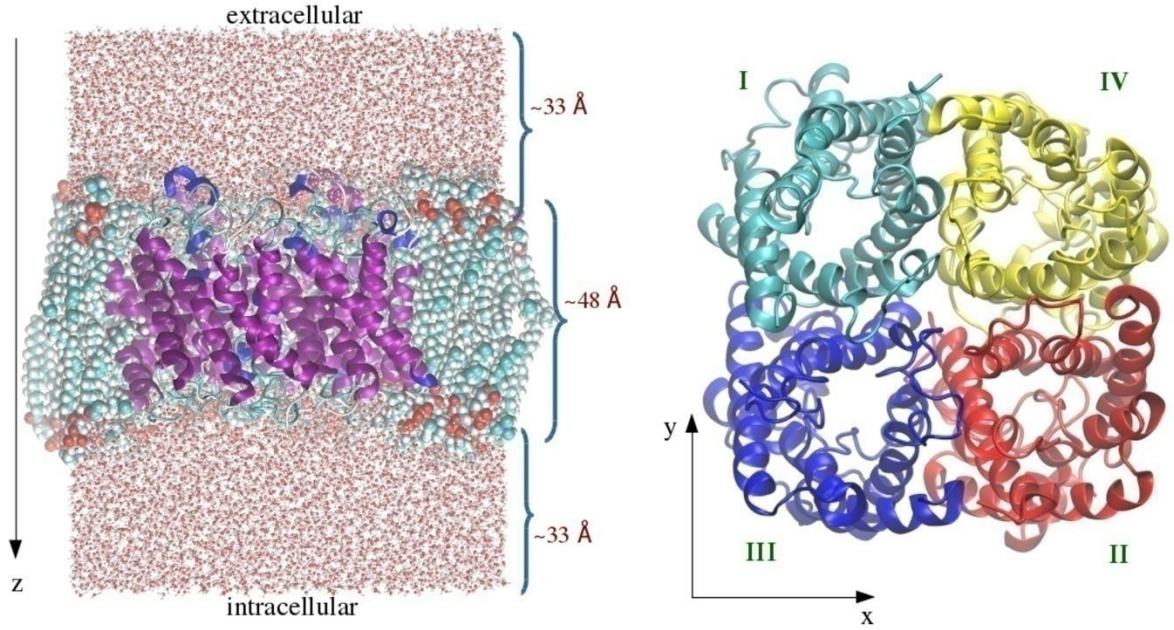

Figure 1. Description of system A. The transmembrane tetramer of AQP3 (left): water, POPC, and protein reported in ball-and-sticks, CPK, and cartoon representation, respectively; (right) labelling of AQP3 monomers.

The AQP3 monomers were numbered from **I** to **IV** and placed as indicated (Figure 1): **I** is the non-covalently or coordinatively bound AQP3 monomer by the gold complex in either B or C systems, respectively.

Root mean square deviation (rmsd) of the backbone atom coordinates showed the stabilization gained upon adequate elongation of the production dynamics, depending on the binding state (Figure. S2). System A and C stabilized after 200-250 ns, whereas system B required approximately 100 ns, so that whole simulation time of A, B and C systems was 400, 200, and 400 ns, respectively. The last 100 ns of trajectory, assumed to be representative of the equilibrated system, was selected in all cases for the subsequent analyses of the dynamic properties of system.

Comparison of the last snapshot structures of A-C trajectories shows how binding of Aubipy alters the shape and size of the water channel. In the non-covalently bound system, $[Aubipy(OH)Cl]^{+}$ binds at the extracellular entrance of the pore, but it does not appreciably alter the conformational arrangement of the selective filter (SF) domain. Instead, it causes a decrease in the pore size (Figure 2). On the other hand, coordinative binding of $[Aubipy(OH)]^{2+}$ at C40 side chain induces both a restriction of the pore size in proximity of the SF domain and, more importantly, an alteration of side

chain conformations of the SF residues. Specifically, it can be noticed the almost 90° rotation of F63 phenyl ring compared to B system, that essentially closes the channel (Figure 2).

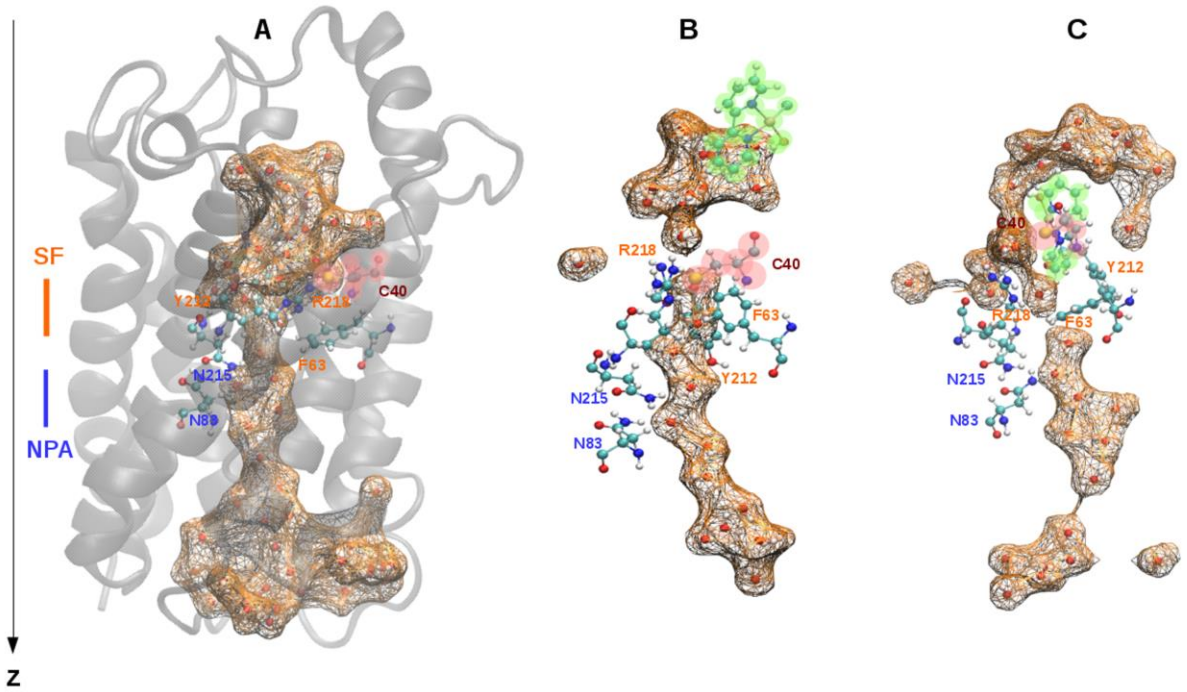

Figure 2. Sketches of the AQP3 domains important for the channel functionality and confined water surface retrieved from the last snapshot structures of A (unbound AQP3), B (non-covalent gold adduct), and (coordinative gold adduct) C trajectories, respectively. Metal complex and C40 atoms are green and pink shaded, respectively.

To better estimate the effects of $[AubipyCl(OH)]^+$ binding on the channel functionality and to take into account for the thermal fluctuation of the system, the water flux across monomer **I** was monitored in the equilibrated segment of A-C trajectories. The average radius of the channel in the transmembrane direction (z axis) was calculated by using the program HOLE. [35] The radius profiles calculated for the unbound AQP3 monomer were in agreement with those already reported for GlpF and AQP2.[48]In the A system, a minimum value of about 1 Å was detected for channel radius at the SF domain, whereas it increases to about 2.5 Å in the NPA domain. On the other hand, the channel radius profiles of the bound systems B and C adopt lower values mainly in the proximity of the SF domain (Figure 3). The channel radius decrease detected in SF domain of B and C system was about

0.25 and 0.5 Å, respectively, thus substantially in agreement with the qualitative sketch gained from snapshot structures (Figure 2).

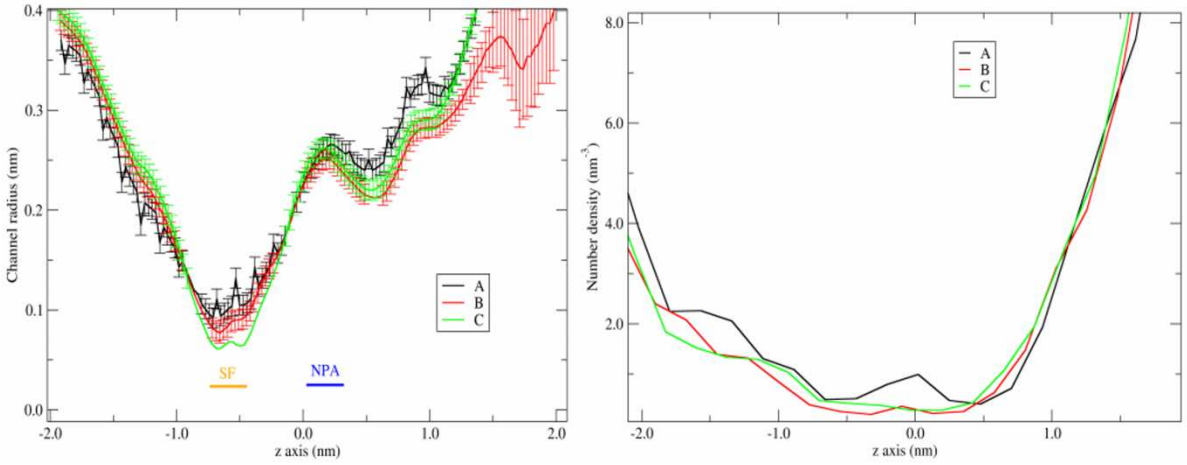

Figure 3. The average channel radius along the transmembrane direction (z axis) of system A, B, and C (left). The number of water molecules per volume units across the z axis (right).

The density of water permeation was also analyzed as described in the experimental section. All A-C systems are characterized by a minimum of water density in the trans-channel region. However, the gold bound states B and C systems presented generally lower density of water, and, consistently with the profiles of channel radius, a more pronounced decrease was detected around z = –1.5 nm (region of $[AubipyCl(OH)]^+$ binding) and z = 0 nm (NPA motif) (Figure 3, right). By analyzing the mean displacement of the confined water (see Experimental Section) we also estimated the water flux of monomer **I** being 4.51, 0.151, and 1.81 (expressed in 1×10^{-14} cm^3 s^{-1} units) for system A, B, and C, respectively. Notably, the calculated values of the water flux in the "gold-free" monomer, are in line with previously reported MD studies. [49]

Our calculations evidenced that, unexpectedly, non-covalent binding is even more effective than covalent binding in reducing the water flux.

The protein conformations representative of the non-covalently and covalently bound AQP3 status were then extrapolated from the B and C trajectories, respectively, using a clustering approach (see Methods). Subsets of four (B1-B4) and two (C1 and C2) conformations were obtained by clustering of B and C trajectories, respectively. By comparison of B1-B4 structures, we noticed that $[Aubipy(OH)Cl]^+$ non-covalent binding takes place in a wide portion of space and with diverse patterns of protein-ligand interactions as displayed by the quite variable orientation of the metal

complex detected in the four models (see Supporting Information). The most representative form, B1, is characterized by π-stacking between the phenyl ring of F136 and the Aubipy(OH)Cl^+ metallacycle (r0), and by polar contact between the carbonyl oxygen (bearing a partial negative charge) of V47 and the positively charged Au(III) metal centre (Figure 4). Notably, F136 and V47 hydrophobic contacts were also detected in B2-B4 conformations, thus, highlighting their importance in the non-covalent binding of Au(III) bipyridyl complexes. The pyridyl rings of [Aubipy(OH)Cl]$^+$, i.e. r1 and r2 indicating the one in *trans* to hydroxo and chlorido ligand, respectively, are differently exposed to the water. Indeed, we detected 7-8 water molecules closely surrounding r2 whereas r1 is mainly involved in hydrophobic contacts with V47 (Figure 4).

On the other hand, C1 and C2 system conformations (coordinative binding) were characterized by almost the same Aubipy-protein interactions, probably because the thiol group of C40 assumed almost the same orientation in the Au(III) coordination. We noticed, in both C1 and C2 conformations, that r1 ring points towards and makes interactions with the SF region residues FF63 and I59, whereas the pyridyl ring in *trans* to coordinated S atom (r2) points towards the extracellular side and is characterized by a higher solvent exposure (Figure 4). Interestingly, this result resembles the solvent exposure detected in the B1 system, with r1 involved in hydrophobic interactions and r2 more exposed to the solvent. It is also worth noting the position of F63 aromatic ring with respect to the r2 of Aubipy(OH), that permits T-shaped rather than π-stacking interaction between these two six-membered rings (Figure 4, right).

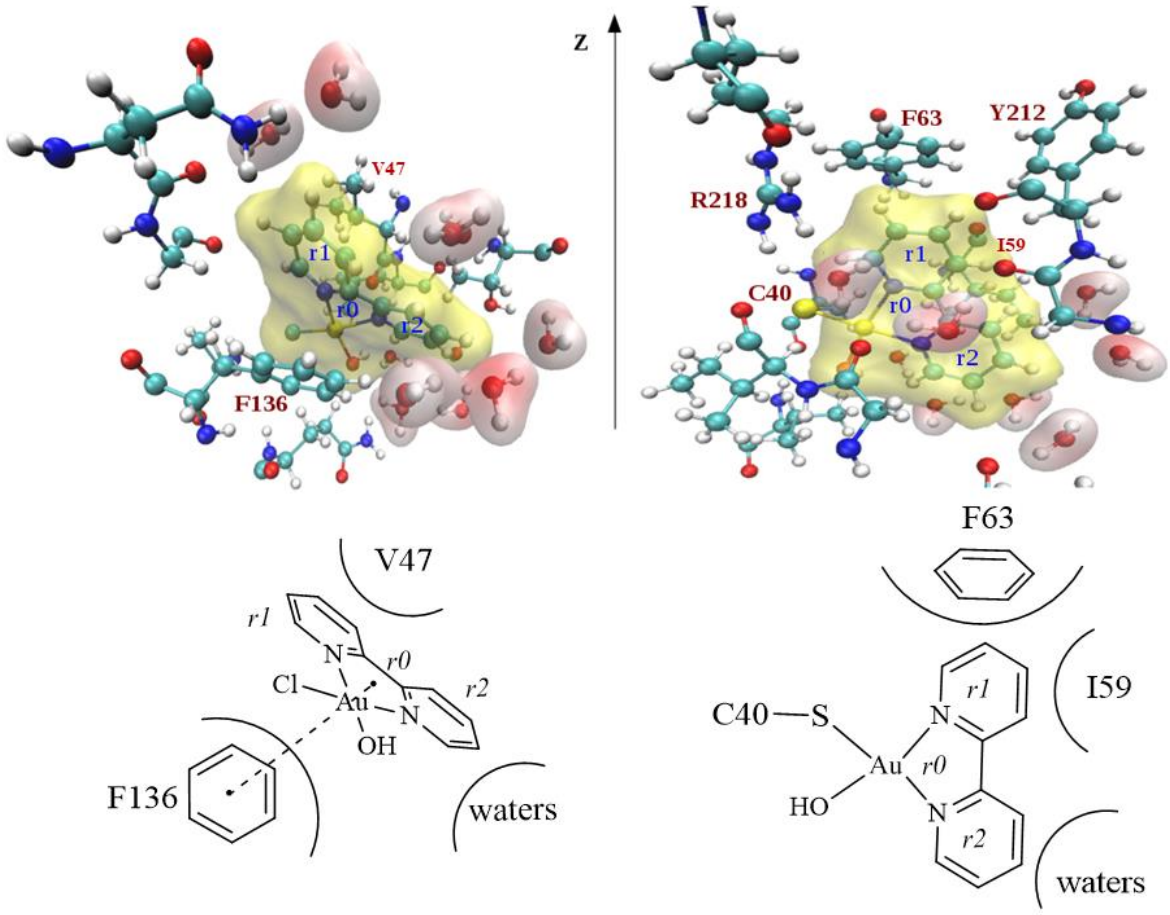

Figure 4. Detailed view of non-covalent B1 (left), and coordinative C1(right) binding states. Top: Water molecules and protein sidechain residues within 3.0 Å of $[AubipyCl(OH)]^+$ molecule (yellow) are reported in ball-and-sticks. The stacking interaction between the phenyl ring of F136 and the Au(III) metallocycle (r0) is reported (dotted line). Condensed rings of the Aubipy(OH) moiety are labeled (r0, r1 and r2). Bottom: 2D schemes of the detected target-ligand interactions are also reported.

Beside the above mentioned conformational rearrangement of F63 side chain, we found that the hydrogen bond patterns involving R218 side chain are responsive to either coordinative or non-covalent binding of $[Aubipy(OH)Cl]^+$. Indeed, the analysis of hydrogen bond frequencies (see Methods) for the side chain N–H bonds (donor) and the main chain carbonyl oxygen (acceptor) of R218 indicated that this residue assumes a folded conformation in systems B and C favouring an additional intra-residue hydrogen bond N_1–H···O (Scheme 5). On the other hand, the R218 conformation tended to be more extended in the unbound A system, i.e. no intra-residue hydrogen bond was detected, and more exposed to the water flux as indicated by the formation of hydrogen bonds between water and either N_1, N_2, Nε, or main chain carbonyl oxygen (Scheme 5). These results

were further corroborated by clustering the A-C trajectories with respect to R218 conformation (Figure S3).

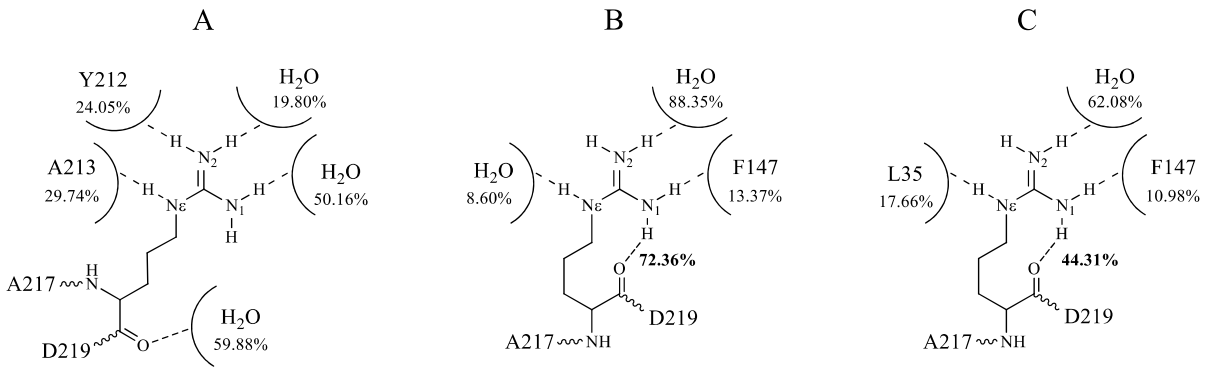

Scheme 5. Hydrogen bond patterns of R218 with the corresponding frequencies (percentage) detected in last 100 ns of A-C systems trajectories. Percentages of intra-residue hydrogen bonds are reported in bold.

Aubipy(OH)-AQP3 interactions: QM/MM calculations. To validate the results obtained by MD, a QM/MM scheme was used to optimise the geometry of B1 and C1 forms of the AQP3-Aubipy complex obtained from MD simulations, with results summarised in Table 1. Both B1 and C1 systems were partitioned into reduced models by including the $[Aubipy(OH)Cl]^+$ complex (B1) or Aubipy(OH) moiety (C1) plus 61 amino acid residues and 8–11 water molecules selected within a radius of approximately 4 Å from the metal fragment. In general, results from QM/MM and purely MM descriptions of the Au(III) centre are in good agreement: differences in bond lengths between the two approaches is typically less than 2%, and angles within 5% (Table 1). Deviations from this trend are seen for the O-Au-Cl (B1) and O-Au-S (C1) angle, which QM/MM predicts to be close to 90° in both forms, unlike MM which predicts a much larger value in C1 than in B1. QM/MM also finds a larger value for the Au-S-C angle in C1, which is rather small in the MM geometry. Overall, QM/MM data support the use of AMBER parameters for description of Aubipy and its interaction with C40 of AQP3. Table 1 also allows comparison of the coordination geometry of Aubipy between gas-phase, unbound and bound environments, and shows that changes between these forms are generally rather small.

Table 1. Comparison of AMBER and QM/MM geometry of B1 and C1 forms.

	Aubipy QM	B1 MM	B1 QM/MM	C1 MM	C1 QM/MM
Au-Cl or S	2.305	2.330	2.312	2.370	2.343
Au-N1	2.074	2.077	2.072	2.128	2.115
Au-N2	2.094	2.107	2.100	2.123	2.069
Au-O	1.967	1.969	1.985	1.965	1.982
S-C	na	na	na	1.820	1.849
N-Au-N	79.5	76.0	79.4	76.8	79.3
N-Au-O	90.2	94.4	93.5	89.6	92.5
O-Au-Cl or S	91.6	83.0	91.9	96.7	93.1
Au-O-H	109.6	108.4	107.3	105.1	108.1
Au-S-C	na	na	na	72.6	92.8

To further examine the importance of non-covalent interactions in the unbound complexes, we examined the QM/MM optimized geometry of B1 in more detail. NBO analysis indicates significant interactions between formally filled orbitals on Au and empty π^* orbitals on F136, the largest totalling 162.8 kJ mol^{-1}. Interactions between π-orbitals on bipy and π^* orbitals on F136 are also present but rather weaker, the largest being 29.7 kJ mol^{-1}. QTAIM analysis finds three bond critical points connecting Aubipy with F136, made up of C$\cdots$C, C$\cdots$Cl and C$\cdots$Au contacts, in addition to numerous contacts with water molecules. In agreement with the findings from MD simulation, all direct contacts between Aubipy and F136 are concentrated at r0, with water contacts around r2. Finally, counterpoise corrected binding energy between F136 and either Aubipy or just bipy were calculated at the w-B97XD/6-31+G(d,p)-SDD level, and found F136$\cdots$Aubipy stabilization to be –39.8 kJ mol^{-1}, whereas that to bipy ligand alone is just –12.0 kJ mol^{-1}, demonstrating the importance of Au-coordination for effective non-covalent binding.

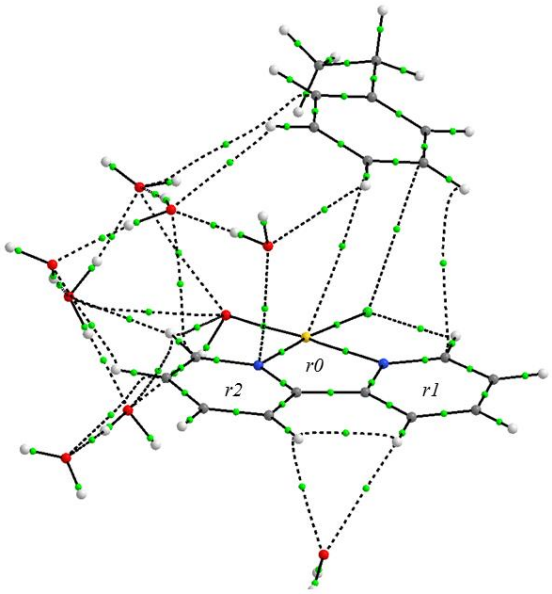

Figure 5 Molecular graph of central section of B1, with electron density at stacking critical points shown.

Conclusions

Numerous studies over the past several years have disclosed important functions of aquaglyceroporins. Although our understanding of their physiological and pathophysiological roles is still in the early stages, there is emerging evidence that these membrane proteins may become exciting new pharmaceutical targets for the treatment of several diseases. Here, we investigated the chemical processes responsible of the biological activity of a gold(III) complex known to be a selective modulator of the aquaglyceroporin AQP3. [8] In particular, we investigated both its interaction with the physiological medium and its binding at the extracellular pore of AQP3 to obtain detailed description of the chemical processes responsible for Aubipy-AQP3 binding. Initially, we developed a scheme for the estimation of thermodynamics and kinetics of aquation and thiol binding of Aubipy from accurate quantum chemistry (Scheme 1), designed to improve the estimation of equilibrium and kinetic constants for the reaction of bipyridyl Au(III) complexes with nucleophiles bearing an acidic proton. As reported elsewhere, [8] the highly charged Au(III) centre strongly increases the acidity of bound nucleophiles, thus favouring the formation of the corresponding deprotonated species. Our calculations showed that aquation or thiol binding of Aubipy leads to deprotonation and formation of the corresponding hydroxo or thiolate species, respectively.

Based on these considerations, we propose that the presence of thiol binding sites in AQP3 is necessary but not sufficient to determine the selectivity of Aubipy. Instead, the formation of stable non-covalent Aubipy-AQP3 adducts is required to compensate the thermodynamic and kinetic barriers associated with the formation of the final covalent adduct. In detail, the overall Aubipy-AQP3 binding process may be depicted as:

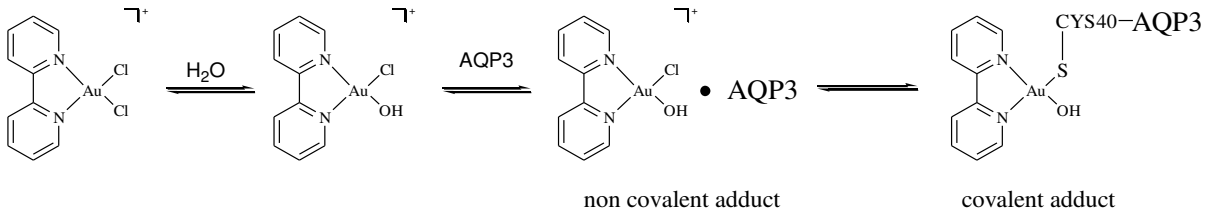

The structures of both non-covalent and covalent Aubipy-AQP3 adducts were investigated by the use of classical molecular dynamics (MD) simulations to gain a detailed insight into the Aubipy binding and its consequences on the AQP3 functionality. By the simulation of unbound, non-covalently bound, and covalently bound systems, namely A, B and C, respectively, we were able to deduce significant structural and functional alterations induced on AQP3 by the gold compound binding. Interestingly, the extracellular pore of both B and C undergoes shape and size alteration that reduces the amount of fluxing water molecules. This observation is corroborated by analysis of the channel radius and water density along the transmembrane direction, and by estimation of the water flux of the AQP3 monomer **I**, bound to gold. Notably, the binding of the gold complex in B and C caused a shrinkage of the pore in the extracellular side, thus, preventing water permeability.

Non-covalent binding of $[Aubipy(OH)Cl]^+$ takes place on the edges of extracellular pore of AQP3 and, more precisely, within the 48-55 and 133-156 loops,[50] with F136 in the latter loop forming π-stacking interactions with the five-membered metallacycle of $[Aubipy(OH)Cl]^+$. The B system trajectory showed how the metal complex spans a large spatial portion of the extracellular pore, with at least four different possible orientations, all maintaining hydrophobic contacts with F136 by the involvement of pyridyl ring in *trans* to hydroxo ligand (r1).

Coordinative binding of $[Aubipy(OH)]^{2+}$ at C40 takes place more deeply in proximity of the SF domain, hence in a narrower portion of the channel. The structure of the Aubipy(OH)-AQP3 covalent adduct is characterized by the interaction of the bipyridyl moiety with F63 and Ile59, which are oriented to form hydrophobic contacts with the r1 ring of the Aubipy(OH) moiety. The aromatic ring of F63 is particularly affected through the formation of a T-shaped interaction with the r1 ring of

Aubipy(OH) moiety. This interaction pattern is probably responsible of the conformational rearrangement of the SF domain that eventually limits water flux. Therefore, our models show that in both B1 and C1 systems (Figure 4), the pyridyl ring r2 is exposed to the water bulk, suggesting that the decoration of Aubipy with hydrophilic groups on r2 ring should increase stabilization of the resulting adduct. Instead, enhancement of the Au(III) complex binding may be attained by optimizing the π-stacking and/or hydrophobic interactions involving the ring r1. Beside the conformational rearrangements of AQP3 residues directly involved in the binding of metal complex, we also determined the response of R218 side chain to either covalent or non-covalent binding of Aubipy. Being the polar component of the so-called ar/R filter, R218 side chain is expected to play a pivotal mechanistic role in the transit of either glycerol or water molecules, mainly through the formation of hydrogen bonds. Consequently, its conformational arrangement is expected to be strictly connected to the channel functionality.

Overall, our results and interpretation are in agreement with a recent work of Almeida et al. [12] showing that the covalent binding of an Au(III) complex at the C40 side chain prevents R218 from forming a H-bond with the protein backbone, which in turn pushes the side-chain into the channel area.

Finally, detailed analyses of the Aubipy(OH)-AQP3 interactions detected in the B1 and C1 structures were then carried out by using QM/MM approaches that provided for an accurate description of the metal fragment and its interacting residues. The QM/MM optimised structures of B1 and C1 closely resemble the corresponding MD structures, thus giving support to the Amber parameter set employed to describe the bipyridyl Au(III) metal moiety. The Aubipy-AQP3 interactions detected in the MD structures of B1 and C1 were also found in the corresponding QM/MM geometries. In particular, stacking interactions between F136 and r0 metallacycle ring are observed in NBO and QTAIM data, while exposure of r2 to water is also apparent. In conclusion, the obtained results will be of extreme value to design new Au(III) complexes as selective AQP3 inhibitors, for example allowing to select aromatic ligands with asymmetric substitution pattern at the two r1 and r2 sides which may further stabilize the coordinative adduct. Specifically, the r2 rings could be substituted with hydrophilic groups such as NH_2, OH, OMe residues in different positons of the bipyridyl ring. Furthermore, careful fine-tuning of the interactions between the metallacycle and F136 leading to the non-covalent adduct formation – achieved again by different substituents on the bipy rings, as well as by the use of different aromatic scaffolds (e.g. C^N cyclometallated and benzymidazole ligands) - may increase the selectivity of the compound for inhibition of AQP3 with respect to other aquaglyceroporin isoforms. Ongoing studies in our labs are testing these possibilities to validate the *in silico* predictions.

References

[1] G. Soveral, S. Nielsen, A. Casini, *Aquaporins in health and disease: new molecular targets for drug discovery*, Eds. CRC Press, Taylor & Francis Group, **2016**.

[2] T. Walz, Y. Fujiyoshi, A. Engel, The AQP structure and functional implications. *Handb. Exp. Pharmacol.* **2009**, *190*, 31-56.

[3] M. Hara-Chikuma, A. S.Verkman, Aquaporin-3 facilitates epidermal cell migration and proliferation during wound healing. *J. Mol. Med.* **2008**, *86*, 221-231.

[4] K. Nakahigashi, K. Kabashima, A. Ikoma, A. S. Verkman, Y. Miyachi, M. Hara-Chikuma, Upregulation of aquaporin-3 is involved in keratinocyte proliferation and epidermal hyperplasia. *J. Invest. Dermatol.* **2011**, *131*, 865-873.

[5] A. Li, D. Lu, Y. Zhang, J. Li, Y. Fang, F. Li, J. Sun, Critical role of aquaporin-3 in epidermal growth factor-induced migration of colorectal carcinoma cells and its clinical significance. *Oncol. Rep.* **2013**, *29*, 535-540.

[6] M. C. Papadopoulos, S. Saadoun, Key roles of aquaporins in tumor biology. *Biochim. et Biophys. Acta* **2015**, *1848*, 2576–2583.

[7] G. Soveral, A. Casini, Aquaporin modulators: a patent review (2010-2015). *Expert Opin. Ther. Pat.* **2017**, *27*, 49-62.

[8] A. P. Martins, A. Marrone, A. Ciancetta, A. Galán Cobo, M. Echevarría, T. F. Moura, N. Re, A. Casini, G. Soveral, Targeting Aquaporin Function: Potent Inhibition of Aquaglyceroporin-3 by a Gold-Based Compound. *PLoS ONE* **2012**, *7*, e37435.

[9] A. de Almeida, G. Soveral, A. Casini, Gold compounds as aquaporin inihibitors: new opportunities for therapy and imaging. *Med. Chem. Commun.* **2014**, *5*, 1444-1453.

[10] A. P. Martins, A. Ciancetta, A. de Almeida, A. Marrone, N. Re, G. Soveral, A. Casini, Aquaporin Inhibition by Gold(III) Compounds: New Insights. *ChemMedChem* **2013**, *8*, 1086–1092.

[11]A. Serna, A. Galán-Cobo, C. Rodrigues, I. Sánchez-Gomar, J. J. Toledo-Aral, T. F. Moura, A. Casini, G. Soveral, M. Echevarría, Functional Inhibition of Aquaporin-3 With a Gold-Based Compound Induces Blockage of Cell Proliferation. *J. Cell. Physiol.* **2014**, *229*, 1787–1801.

[12]A. de Almeida, A. F. Mósca, D. Wragg, M. Wenzel, P. Kavanagh, G. Barone, S. Leoni, G. Soveral, A. Casini, The mechanism of aquaporin inhibition by gold compounds elucidated by biophysical and computational methods. *Chem. Commun.* **2017**, *53*, 3830-3833.

[13] A. de Almeida, B. L. Oliveira, J. D.G. Correia, G. Soveral, A. Casini, Emerging protein targets for metal-based pharmaceutical agents: An update. *Coord. Chem. Rev.* **2013**, *257*, 2689-2704.

[14]Y. Hirano, N. Okimoto, I. Kadohira, M. Suematsu, K. Yasuoka, M. Yasui, Molecular mechanisms of how Mercury inhibits water permeation through Aquaporin-1: Understanding by molecular dynamics simulation. *Biophys J.* **2010**, *98*, 1512-1519. L. Janosi, M. Ceccarelli, The gating mechanism of the human Aquaporin 5 revealed by molecular dynamics simulations. *PLoS One* **2013**, *8*, e59897. S. Kaptan, M. Assentoft, H. P. Schneider, R. A. Fenton, J. W. Deitmer, N. MacAulay, B. L. de Groot, H95 is a pH-dependent gate in Aquaporin 4. *Structure* **2015**, *23*, 2309-2318.

[15]Gaussian 09, Revision D.01, M. J. Frisch, G. W. Trucks, H. B. Schlegel, G. E. Scuseria, M. A. Robb, J. R. Cheeseman, G. Scalmani, V. Barone, B. Mennucci, G. A. Petersson, H. Nakatsuji, M. Caricato, X. Li, H. P. Hratchian, A. F. Izmaylov, J. Bloino, G. Zheng, J. L. Sonnenberg, M. Hada, M. Ehara, K. Toyota, R. Fukuda, J. Hasegawa, M. Ishida, T. Nakajima, Y. Honda, O. Kitao, H. Nakai, T. Vreven, J. A. Montgomery, Jr., J. E. Peralta, F. Ogliaro, M. Bearpark, J. J. Heyd, E. Brothers, K. N. Kudin, V. N. Staroverov, T. Keith, R. Kobayashi, J. Normand, K. Raghavachari, A. Rendell, J. C. Burant, S. S. Iyengar, J. Tomasi, M. Cossi, N. Rega, J. M. Millam, M. Klene, J. E. Knox, J. B. Cross, V. Bakken, C. Adamo, J. Jaramillo, R. Gomperts, R. E. Stratmann, O. Yazyev, A. J. Austin, R. Cammi, C. Pomelli, J. W. Ochterski, R. L. Martin, K. Morokuma, V. G. Zakrzewski, G. A. Voth, P. Salvador, J. J. Dannenberg, S. Dapprich, A. D. Daniels, O. Farkas, J. B. Foresman, J. V. Ortiz, J. Cioslowski, and D. J. Fox, Gaussian, Inc., Wallingford CT, **2013**.

[16]A. D. Becke, Density-functional thermochemistry. III. The role of exact exchange. *J. Chem. Phys.* **1993**, *98*, 5648-5652.

[17]S. Q. Niu, M. B. Hall, Theoretical studies of reactions of transition-metal complexes. *Chem. Rev.* **2000**, *100*, 353–405.

[18]basis set: T. H. Dunning Jr., P. J. Hay, in *Modern Theoretical Chemistry*, *Vol. 3*, (Ed.: H. F. Schaefer III), Plenum, New York, **1977**, pp 1-28. pseudopotential: a) P. J. Hay, W. R. Wadt, Ab initio effective core potentials for molecular calculations - potentials for the transition-metal atoms Sc to Hg. *J. Chem. Phys.* **1985**, *82*, 270-283; b) W. R. Wadt, P. J. Hay, Ab initio effective core potentials for molecular calculations - potentials for main group elements Na to Bi. *J. Chem. Phys.* **1985**, *82*, 284-298; c) P. J. Hay, W. R. Wadt, Ab initio effective core potentials for molecular calculations - potentials for K to Au including the outermost core orbitals. *J. Chem. Phys.* **1985**, *82*, 299-310.

[19]a) R. Ditchfield, W. J. Hehre, J. A. Pople, Self-Consistent Molecular Orbital Methods. 9. Extended Gaussian-type basis for molecular-orbital studies of organic molecules. *J. Chem. Phys.* **1971**, *54*, 724; b) M. M. Francl, W. J. Pietro, W. J. Hehre, J. S. Binkley, D. J. DeFrees, J. A. Pople, M. S. Gordon, Self-Consistent Molecular Orbital Methods. 23. A polarization-type basis set for 2nd-row elements. *J. Chem. Phys.* 1**982**, *77*, 3654-3665; c) V. A. Rassolov, M. A. Ratner, J. A. Pople, P. C. Redfern, L. A. Curtiss, 6-31G* Basis Set for Third-Row Atoms. *J. Comp. Chem.*, **2001**, *22*, 976-984.

[20]M. Cossi, N. Rega, G. Scalmani, V. Barone, Energies, structures, and electronic properties of molecules in solution with the C-PCM solvation model. *J. Comp. Chem.* **2003**, *24*, 669-681.

[21]A. D. McLean, G. S. Chandler, Contracted Gaussian-basis sets for molecular calculations. 1. 2nd row atoms, Z=11-18. *J. Chem. Phys.* **1980**, *72*, 5639-48.

[22]Corresponding to the Hay-Wadt basis set [18] with no contraction.

[23]J. K.-C. Lau, D. V. Deubel, Hydrolysis of the anticancer drug Cisplatin: pitfalls in the interpretation of quantum chemical calculations. *J. Chem. Theory Comput.* **2006**, *2*, 103-106.

[24]J. Wang, P. Cieplak, P. A. Kollman, How well does a restrained electrostatic potential (RESP) model perform in calculating conformational energies of organic and biological molecules? *J. Comp. Chem.* **2000**, *21*, 1049–1074.

[25]S. Pall, M. J. Abraham, C. Kutzner, B. Hess, E. Lindahl, *Tackling exascale software challenges in molecular dynamics simulations with GROMACS.* in *Solving Software Challenges for Exascale*, *Vol. 8759* (Eds.: S. Markidis, E. Laure), Springer International Publishing Switzerland, London, **2015**, pp. 3–27.

[26]A. Spinello, A. de Almeida, A. Casini, G. Barone, The inhibition of glycerol permeation through aquaglyceroporin-3 induced by mercury(II): A molecular dynamics study. *J. Inorg. Biochem.* **2016**, *160*, 78-84.

[27]S. Jo, T. Kim, V.G. Iyer, W. Im, CHARMM-GUI: A web-based graphical user interface for CHARMM. *J. Comput. Chem.* **2008**, *29*, 1859–1865.

[28]E.L. Wu, X. Cheng, S. Jo, H. Rui, K.C. Song, E.M. Dávila-Contreras, Y. Qi, J. Lee, V. Monje-Galvan, R.M. Venable, J.B. Klauda, W. Im, CHARMM-GUI Membrane Builder toward realistic biological membrane simulations. *J. Comput. Chem.* **2014**, *35*, 1997–2004.

[29]S. Nosè, A molecular dynamics method for simulations in the canonical ensemble. *Mol. Phys.*, **1984**, *52*, 255–268. W. G. Hoover, Canonical dynamics: equilibrium phase-space distributions. *Phys. Rev. A*, **1985**, *31*, 1695–1697.

[30]M. Parrinello, A. Rahman, Polymorphic transitions in single crystals: A new molecular dynamics method. *J. Appl. Phys.* **1981**, *52*, 7182–7190. S. Nosè, M. L. Klein, Constant pressure molecular dynamics for molecular systems. *Mol. Phys.* **1983**, *50*, 1055–1076.

[31]B. Hess, H. Bekker, H. J. C. Berendsen, J. G. E. M. Fraaije, LINCS: A Linear Constraint Solver for molecular simulations. *J. Comp. Chem.* **1997**, *18*, 1463-1472.

[32]U. Essmann, L. Perera, M. L. Berkowitz, T. Darden, H. Lee, L. G. Pedersen, A smooth particle mesh Ewald method. *J. Chem. Phys.* **1995**, *103*, 8577-8592.

[33]W. Humphrey, A. Dalke, K. Schulten, VMD: Visual molecular dynamics. *J. Molec. Graphics* **1996**, *14*, 33-38.

[34]Maestro, version 9.4, Schrödinger, LLC, New York, NY, 2013.

[35]a) O. S. Smart, J. M. Goodfellow, B. A. Wallace, The Pore Dimensions of Gramicidin A. *Biophys. J.* **1993**, *65*, 2455-2460.; b) O. S. Smart, J. G. Neduvelil, X. Wang, B. A. Wallace, M. S. P. Sansom, HOLE: A program for the analysis of the pore dimensions of ion channel structural models. *J. Molec. Graphics* **1996**, *14*, 354-360.

[36]F. Zhu, F. E. Tajkhorshid, K. Schulten, Collective diffusion model for water permeation through microscopic channels. *Phys. Rev. Lett.* **2004**, *93*, 224501-224504.

[37]M. Hashido, A. Kidera, M. Ikeguchi, Water transport in Aquoporins: Osmotic permeability matrix analysis of molecular dynamics simulations. *Biophys. J.* **2007**, *93*, 373-385.

[38]X. Daura, K. Gademann, B. Jaun, D. Seebach, W. F. van Gunsteren, A. E. Mark, Peptide folding: when simulation meets experiment. *Angew. Chem. Int. Ed.* **1999**, *38*, 236–240.

[39]T. Vreven, K.S. Byun, I. Komáromi, S. Dapprich, J.A. Montgomery Jr., K. Morokuma, M.J. Frisch, Combining quantum mechanics methods with molecular mechanics methods in ONIOM. *J. Chem. Theory Comput.* **2006**, *2*, 815–826.

[40]W. D. Cornell, P. Cieplak, C. I. Bayly, I. R. Gould, K. M. Merz Jr., D. M. Ferguson, D. C. Spellmeyer, T. Fox, J. W. Caldwell, P. A. Kollman, A 2nd generation force-field for the

simulation of proteins, nucleic acids and organic molecules. *J. Am. Chem. Soc.* ***1995****, 17*, 5179–5197.

[41]a) W. J. Hehre, R. Ditchfield, J. A. Pople, Self-consistent molecular orbital methods 12 Further extensions of Gaussian-type basis sets for use in molecular orbital studies of organic molecules. *J. Chem. Phys.* **1972**, *56*, 2257–2261; b) M. J. Frisch, J. A. Pople, J. S. Binkley, Self-consistent molecular orbital methods. 25. Supplementary functions for Gaussian basis sets. *J. Chem. Phys.* **1984**, *80*, 3265–3269; c) D. Andrae, U. Haußerman, M. Dolg, H. Stoll, H. Preuß, Energy adjusted *ab initio* pseudopotentials for the 2nd row and 3rd row transition elements – molecular test for Ag2, Au2, RuH and OsH. *Theor. Chim. Acta* **1990**, *77*, 123–141.

[42]A. E. Reed, L. A. Curtiss, F. Weinhold, Intermolecular interactions from a natural bond orbital, donor-acceptor viewpoint. *Chem. Rev.* **1988**, *88*, 899-926.

[43]R. F. W. Bader, Atoms in Molecules: A Quantum Theory, Clarendon Press, Oxford, **1990**.

[44]J.-D. Chai and M. Head-Gordon, Long-range corrected hybrid density functionals with damped atom-atom dispersion corrections. *Phys. Chem. Chem. Phys.* **2008**, *10*, 6615-6620.

[45]S. F. Boys and F. Bernardi, Calculation of Small Molecular Interactions by Differences of Separate Total Energies – Some Procedures with Reduced Errors. *Mol. Phys.* **1970**, *19*, 553-566.

[46]a) F. Abbate, P. Orioli, B. Bruni, G. Marcon, L. Messori, Crystal structure and solution chemistry of the cytotoxic complex 2,2-dichloro(o-phenantroline) gold(III) chloride. *Inorg. Chim. Acta* **2000**, *311*, 1–5.; b) L. Messori, F. Abbate, G. Marcon, P. Orioli, M. Fontani, E. Mini, T. Mazzei, S. Carotti, T. O'Connell, P. Zanello, Gold(III) complexes as potential antitumor agents: Solution chemistry and cytotoxic properties of some selected gold(III) compounds. *J. Med. Chem.* **2000**, *43*, 3541–3548.; c) A. Casini, G. Kelter, C. Gabbiani, M. A. Cinellu, G. Minghetti, D. Fregona, H.-H. Fiebig, L. Messori, Chemistry, antiproliferative properties, tumor selectivity, and molecular mechanisms of novel gold(III) compounds for cancer treatment: a systematic study. *J. Biol. Inorg. Chem.* **2009**, *14*, 1139–1149.

[47]R. B. Martin, *Platinum complexes: hydrolysis and binding to N(7) and N(1) of purines.* In *Cisplatin: Chemistry and biochemistry of a leading anticancer drug* (Ed.: B. Lippert), Verlag Helvetica ChimicaActa, Zürich, **1999**, pp 183-205.

[48]a) M. Ø. Jensen, E. Tajkhorshid, K. Schulten, Electrostatic Tuning of Permeation and Selectivity in Aquaporin Water Channels. *Biophys. J.* **2003**, *85*, 2884–2899; b) A. R. Binesh, R. Kamali, Molecular dynamics insights into human aquaporin 2 water channel. *Biophys. Chem.* **2015**, *207*, 107-113.

[49]M. Ø. Jensen, O. G. Mouritsen, Single-channel water permeabilities of Escherichia coli aquaporins AqpZ and GlpZ. *Biophys. J.* **2006**, *90*, 2270-2284. T. O. Wambo, R. A. Rodriguez, L. Y. Chen, Computing osmotic permeabilities of aquaporins AQP4, AQP5, and GlpF from near-equilibrium simulations. *Biochim. Biophys. Acta* **2017**, *1859*, 1310-1316.

[50]A. Kirscht, S. S. Kaptan, G. P. Bienert, F. Chaumont, P. Nissen, B. L. de Groot, P. Kjellbom, P. Gourdon, U. Johanson, Crystal Structure of an Ammonia-Permeable Aquaporin. *PLoS Biol.* **2016**, *14*, e1002411.